CHEMISTRY OF MATERIALS

pubs.acs.org/cm

Article

High-Entropy Oxides in the Mullite-Type Structure

Andrea Kirsch,* Espen Drath Bøjesen, Niels Lefeld, Rasmus Larsen, Jette Katja Mathiesen, Susanne Linn Skjærvø, Rebecca Katharina Pittkowski, Denis Sheptyakov, and Kirsten M. Ø. Jensen*

Cite This: *Chem. Mater.* 2023, 35, 8664–8674

Read Online

ACCESS | Metrics & More | Article Recommendations | Supporting Information

ABSTRACT: High-entropy materials (HEMs) represent a new class of solid solutions containing at least five different elements. Their compositional diversity makes them promising as platforms for the development of functional materials. We synthesized new HEMs in a mullite-type structure and present five compounds, i.e., $Bi_2(Al_{0.25}Ga_{0.25}Fe_{0.25}Mn_{0.25})_4O_9$ and $A_2Mn_4O_{10}$ with variations of A = Nd, Sm, Y, Er, Eu, Ce, and Bi, demonstrating the vast accessible composition space. By combining scattering, microscopy, and spectroscopy techniques, we show that our materials are mixed solid solutions. Remarkably, when following their crystallization in situ using X-ray diffraction and X-ray absorption spectroscopy, we find that the HEMs form through a metastable amorphous phase without the formation of any crystalline intermediates. We expect that our synthesis is excellently suited to synthesizing diverse HEMs and therefore will have a significant impact on their future exploration.

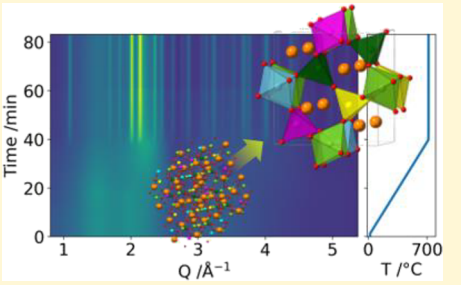

1. INTRODUCTION

Engineering compositional disorder into materials has attracted immense interest since the introduction of the high-entropy (HE) concept and the first intentional synthesis of HE alloys in 2004.[1,2] HE materials contain at least five elements of ca. equal amounts (5−35%)[3] statistically distributed on one crystallographic lattice site and thus form single-phase solid solutions. In 2015,[4] the first high-entropy oxide (HEO) was described. Subsequently several studies proved the vast potential of HEOs by reporting striking properties, such as ultralow thermal conductivity,[5] superionic Li^+ mobility at room temperature,[6] and switchable optical band gaps.[7] It has been pointed out that HEOs crystallize mainly in simple crystal structures,[8,9] and HEOs have been reported in rock-salt,[4] fluorite,[10] spinel,[11] perovskite,[5] and pyrochlore structures.[12] Extending the HE concept to more structurally complex compounds with a variety of different crystallographic sites, types of polyhedral environments, and connectivity may provide new opportunities in material design. With such structures, creating targeted disorder[13] on specific lattice sites or in specific dimensions (1D chains and 2D sheets) would become possible.

We studied the synthetic accessibility of structurally complex mullite-type HEOs, $Bi_2M_4O_9$ (M = Ga^{3+}, Al^{3+}, and Fe^{3+}) and $A_2Mn_4O_{10}$ (A = RE^{3+}, Y^{3+}, and Bi^{3+}). First, their structural diversity is manifold with three distinct crystallographic metal sites, four different metal coordination environments, and a complex connectivity between them (Figure 1a,b). Second, parent compounds of this system exhibit a variety of exciting properties including multiferroicity,[14,15] a unique cooperative catalytic reaction pathway for oxidation of NO,[16] and frustrated magnetism.[17] $Bi_2M_4O_9$ and $A_2Mn_4O_{10}$ crystallize in the orthorhombic space group *Pbam* and are isostructural except that $A_2Mn_4O_{10}$ has double-pyramidal Mn_2O_8 units while $Bi_2M_4O_9$ has double-tetrahedral M_2O_7 units (Figure 1d). These connect edge-sharing MO_6 octahedral chains along *c* (Figure 1c) and build local pentagonal units in the *ab* plane in both compounds (Figure 1e). In $A_2Mn_4O_{10}$, Mn exists in a mixed valence state, and charge ordering occurs where Mn^{3+} is pyramidally coordinated and Mn^{4+} is octahedrally coordinated. Applying the HE concept to this structure type offers an excellent platform for tailoring properties, allows the study of fundamental interactions of magnetic exchange, and bears the potential to discover new physical phenomena. For instance, the long-range magnetic structures[18] and multiferroic properties[19] of the $A_2Mn_4O_{10}$ parents strongly depend on the type of RE. The magnetic behavior might thus be designed in HEO mullite-type materials by rational combinations of REs with varying magnetic moments, as recently demonstrated for spinel HEOs.[20] Using a classical Heisenberg model, Mazza et al. showed that compositionally disordered perovskites paradoxically can possess magnetic uniformity and that magnetic HEOs might not only pave the way to continuous control over ordering and critical temperatures but also to induce highly controllable exchange bias behavior previously only accessible by heterojunctions.[21] Mullite-type materials, furthermore, demonstrate promise in catalysis as $Sm_2Mn_4O_{10}$ has proven

Received: July 24, 2023
Revised: September 18, 2023
Published: October 4, 2023

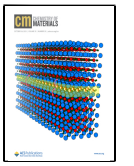

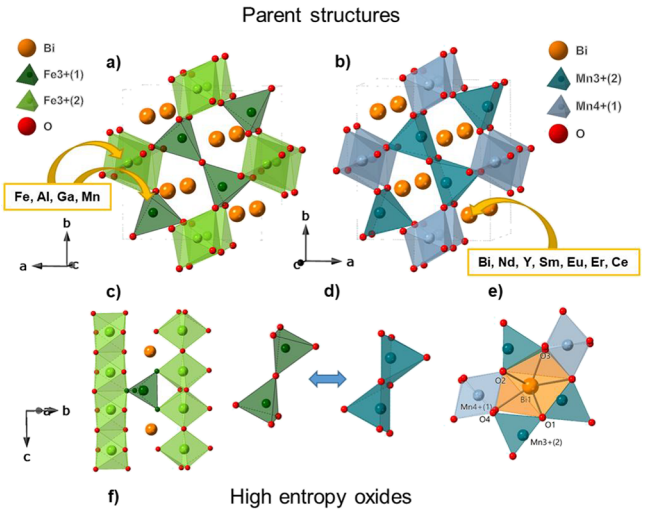

Sample name	Composition
Bi-HEO	$Bi_2(Al_{0.25}Fe_{0.25}Ga_{0.25}Mn_{0.25})_4O_9$
RE-HEO	$(Er_{0.2}Y_{0.2}Sm_{0.2}Nd_{0.2}Eu_{0.2})_2Mn_4O_{10}$
Er-HEO	$(Er_{0.2}Y_{0.2}Sm_{0.2}Nd_{0.2}Bi_{0.2})_2Mn_4O_{10}$
Eu-HEO	$(Eu_{0.2}Y_{0.2}Sm_{0.2}Nd_{0.2}Bi_{0.2})_2Mn_4O_{10}$
Ce-HEO	$(Ce_{0.2}Y_{0.2}Sm_{0.2}Nd_{0.2}Bi_{0.2})_2Mn_4O_{10}$

Figure 1. Crystal structures and polyhedral connectivity of the parent compounds and an overview of the synthesized high-entropy oxides. Unit cells of (a) $Bi_2Fe_4O_9$ and (b) $Bi_2Mn_4O_{10}$. (c) The structures show infinite octahedral chains along the *c*-axis. (d) Structural difference between $Bi_2Fe_4O_9$ and $Bi_2Mn_4O_{10}$ (M_2O_7 or M_2O_8 units). (e) Polyhedral connectivity in the local pentagonal lattice. (f) Overview and nomenclature of the HEOs synthesized in this work.

to be a highly active and stable catalyst for the oxidation of NO through a newly discovered cooperative lattice oxygen redox mechanism involving multiple Mn sites.[16] On this basis, the mullite-type oxide family could be a platform for the design of efficient catalysts with simultaneous strong O binding and activation as well as high thermal stability in harsh conditions.[16] The catalytic effect may even be enhanced in HEO mullite-type materials, as has previously been shown for HE alloys for electrocatalysis.[22,23]

We mapped out the synthetic accessibility and synthesized five prototype compositions. These include one $Bi_2M_4O_9$ ($Bi_2(Al_{0.25}Ga_{0.25}Fe_{0.25}Mn_{0.25})_4O_9$) and four $A_2Mn_4O_{10}$ with A = Nd, Sm, Y, Er, Eu, Ce, and Bi (Figure 1f). We show that the materials are indeed mixed solid solutions using neutron and X-ray powder diffraction (NPD and XRD) with subsequent Rietveld analysis, X-ray total scattering and pair distribution function (PDF) analysis, scanning transmission electron microscopy (STEM)−energy-dispersive X-ray spectroscopy (EDX), and infrared and Raman spectroscopy. We use a sol−gel strategy to produce a nanostructured precursor, which is heated to form the HEOs. We follow this formation using in situ XRD and X-ray spectroscopy (XAS). Surprisingly, even though cocrystallization is common in this system,[24,25] all HEOs form through a metastable amorphous phase without the formation of any crystalline intermediates.

2. RESULTS

2.1. B-Site-Substituted $Bi_2(Al_{0.25}Fe_{0.25}Ga_{0.25}Mn_{0.25})_4O_9$.

We perform a detailed structural analysis of the newly synthesized $Bi_2(Al_{0.25}Fe_{0.25}Ga_{0.25}Mn_{0.25})_4O_9$ (Bi-HEO) and investigate whether this material is a statistically mixed solid solution rather than a simple physical mixture of the parent compounds $Bi_2Al_4O_9$, $Bi_2Ga_4O_9$, $Bi_2Fe_4O_9$, and $Bi_2Mn_4O_{10}$. Comparing the synchrotron XRD data of Bi-HEO and its parent compounds clearly shows significantly shifted reflections, e.g., (001), (121), and (211) as highlighted by gray lines in Figure 2a. The separated (001) reflection shows a symmetrical profile without any observable shoulders (Figure 2b), and the pattern can be excellently fitted with space group *Pbam* using the Pawley method (R_{wp} = 1.9%, Figure S1a). The refined cell dimensions a = 7.782(2) Å, b = 8.368(3) Å, and c = 5.848(2) Å (Table S1) are close to a simple calculated average of the parent compounds in the respective dimension a = 7.7967 Å, b = 8.3631 Å, and c = 5.8472 Å (Table S2). Rietveld refinement using a structural model with equally distributed Mn, Al, Fe, and Ga over the octahedral and tetrahedral sites results in R_{wp} = 4.1% (Figure 2e) and validates the unit cell dimensions as a = 7.7853(7) Å, b = 8.3696(7) Å, and c = 5.8423(6) Å. The refined average crystallite sizes of 57(3) nm (Rietveld) and 70(9) nm (Pawley) suggest rather small coherently scattering domains, despite a long calcination time of 20 h at 700 °C. This implies that the growth of this material is inherently inhibited. A reason could be the significant microstrain that was refined to ε_0 = 0.00302(4). This value is an order of magnitude higher compared to those of the parent compounds calcined for the same amount of time (Table S2) and can be expected[26,27] for such a complex network of differently connected polyhedral environments with differing ionic radii (Al^{3+} 0.53 Å[28] Fe^{3+} 0.79 Å[28]).

Temperature-dependent XRD studies (Figure S2) did not reveal any obvious peaks or shoulders on the HEO reflections. Therefore, we can exclude any hidden impurities with differing thermal expansion behavior.

The parent compounds $Bi_2Fe_4O_9$ and $Bi_2Mn_4O_{10}$ are well-known for their pentagonal frustrated magnetic structures with ordering temperatures of T_N = 244 K[17] and T_N = 39 K.[29] However, the NPD patterns of Bi-HEO do not show the appearance of any long-range magnetic order even when the sample is cooled to 1.7 K. This is seen in Figure 2f,g, where the scattering patterns of Bi-HEO and $Bi_2Fe_4O_9$ are compared in the relevant Q-range. Here, $Bi_2Fe_4O_9$ shows strong magnetic reflections at Q = 1.3 $Å^{-1}$ already at 100 K. In the same region, Bi-HEO shows a magnetic diffuse signal (arrow, Figure 2f) at 1.7 K, indicating a short-range magnetic order. Such a diffuse signal was also reported for $Bi_2Fe_4O_9$ at 280 K, which sluggishly grew into well-defined magnetic Bragg peaks at lower temperatures.[30] The absence of any long-range magnetic order in Bi-HEO provides strong evidence that our material represents a solid solution rather than a mixture of separated phases. Otherwise, the strong magnetic signals of $Bi_2Fe_4O_9$ or $Bi_2Mn_4O_{10}$ would appear below their respective ordering temperatures. A Pawley fit of the 300 K neutron data (Figure S3a) yields an R_{wp} = 4.4% and unit cell dimensions a = 7.77(1) Å, b = 8.37(1) Å, and c = 5.85(1) Å in accordance with the XRD refinements (Table S1). However, magnification of the background shows at least three peaks (Figure S3b), which clearly cannot be explained with the *Pbam* symmetry. Since we did not observe these in the XRD data, we assume that they arise from one or more minor impurity phases in low concentrations containing weak scatterers, e.g., some Al/Ga oxides or hydroxides. Nevertheless, Rietveld refinement of the neutron data (Figure 2h) yields a reasonable R_{wp} = 6.2% and matches the refined a, b, c, and microstrain ε_0 of the XRD data (Table S1). For both data sets, some atomic displacement

https://doi.org/10.1021/acs.chemmater.3c01830
Chem. Mater. 2023, 35, 8664−8674

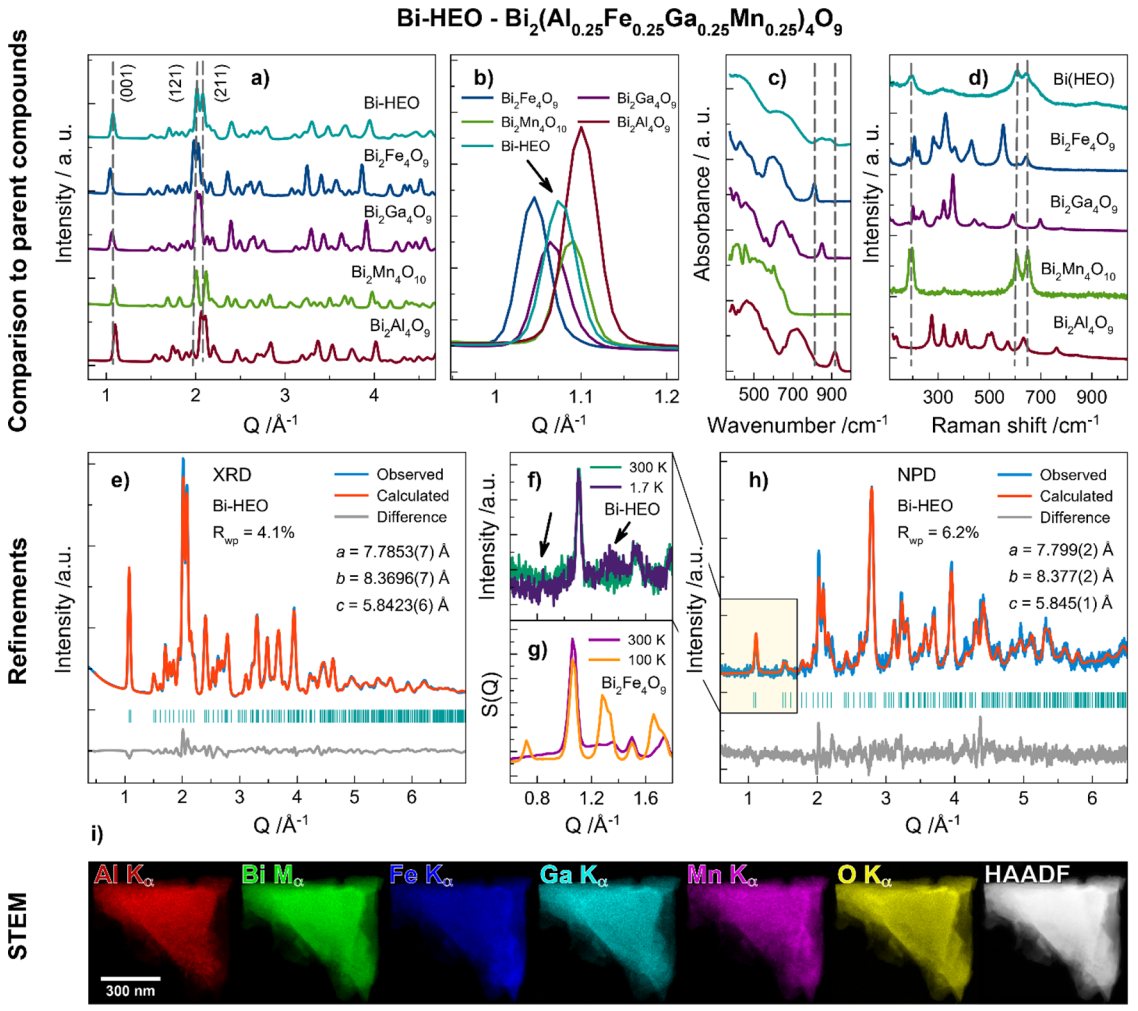

Figure 2. Structural analysis of $Bi_2(Al_{0.25}Ga_{0.25}Fe_{0.25}Mn_{0.25})_4O_9$ (Bi-HEO). (a) Synchrotron X-ray diffraction data. (b) Detailed view of the (001) reflection. (c) Infrared and (d) Raman spectra of Bi-HEO in comparison to parents $Bi_2Al_4O_9$, $Bi_2Ga_4O_9$, $Bi_2Fe_4O_9$, and $Bi_2Mn_4O_{10}$. (e) Rietveld refinement of synchrotron X-ray diffraction data. (f) Comparison between neutron data from Bi-HEO at 300 and 1.7 K and (g) $Bi_2Fe_4O_9$ at 300 and 100 K. (h) Rietveld refinement of neutron powder diffraction data. (i) STEM-EDX analysis of a representative particle of $Bi_2(Al_{0.25}Ga_{0.25}Fe_{0.25}Mn_{0.25})_4O_9$ (Bi-HEO).

parameters (ADPs) refine to quite high values (B_{iso} = 0.4(2)−2.5(2) Å^2), which we relate to the substantial chemical disorder around the sites rather than to abnormally large thermal vibrations. As high-entropy materials contain many elements with different sizes, a slight displacement from their average atomic position in the crystal is expected. In a Rietveld refinement, such a static displacive disorder would add to the displacement caused by thermal vibrations and therefore lead to higher *B*-values. To explore the local structure of Bi-HEO, we collected X-ray total scattering data and performed PDF analysis. Bi-HEO clearly shows shorter correlation lengths compared to its parent compounds (Figure S4). We attribute this to microstrain rather than to size effects since the Rietveld analysis suggests that the average crystallite size is too big to cause any significant damping of the PDFs in the *r*-range available from the X-ray rapid-acquisition (RA)-PDF experiments. In Figure S5, we compare a calculated PDF with 1/4 $Bi_2Fe_4O_9$, 1/4 $Bi_2Al_4O_9$, 1/4 $Bi_2Ga_4O_9$, and 1/4 $Bi_2Mn_4O_{10}$ simulating a simple physical mix of the parent compounds (details in the Methods Section) with the experimental PDF of Bi-HEO. The PDFs are almost identical until ca. 8.4 Å, which is on the order of the dimension of the unit cell. This means that the local structure of the material is well described by a simple mixture of the parents. However, beyond that distance, the PDFs clearly start to differ from each other as the longer range order is more affected by the differing lattice parameters for the parent phases in the simulated physical mixture. The whole range of the Bi-HEO PDF (r = 1−60 Å) is well described (R_{wp}, 18.9%, Figure S6) by the mullite structure. However, individual fits of the *r*-ranges from 1 to 25 Å and from 25 to 60 Å lead to significantly improved fits with R_{wp} values of 15.7 and 11.6% (Figure S7, Table S1). This improvement relates to the increased PDF peak broadening in the high *r*-region and considerably higher refined values for the ADP (e.g., B_{iso} of Bi doubles from 1.1 to 2 Å^2, Table S1). Consistent with the results from the Rietveld analysis, these high ADP values likely represent static disorder around the sites and could be caused by a mismatch of the different ion sizes in the lattice leading to significant microstrain in the material.[26]

To further evaluate the local structure, we collected the infrared (IR) (Figure 2c) and Raman (Figure 2d) spectra of Bi-HEO and its parent phases. The IR spectrum of mullite-type materials can be divided into three main regions: 400−

https://doi.org/10.1021/acs.chemmater.3c01830
Chem. Mater. 2023, 35, 8664−8674

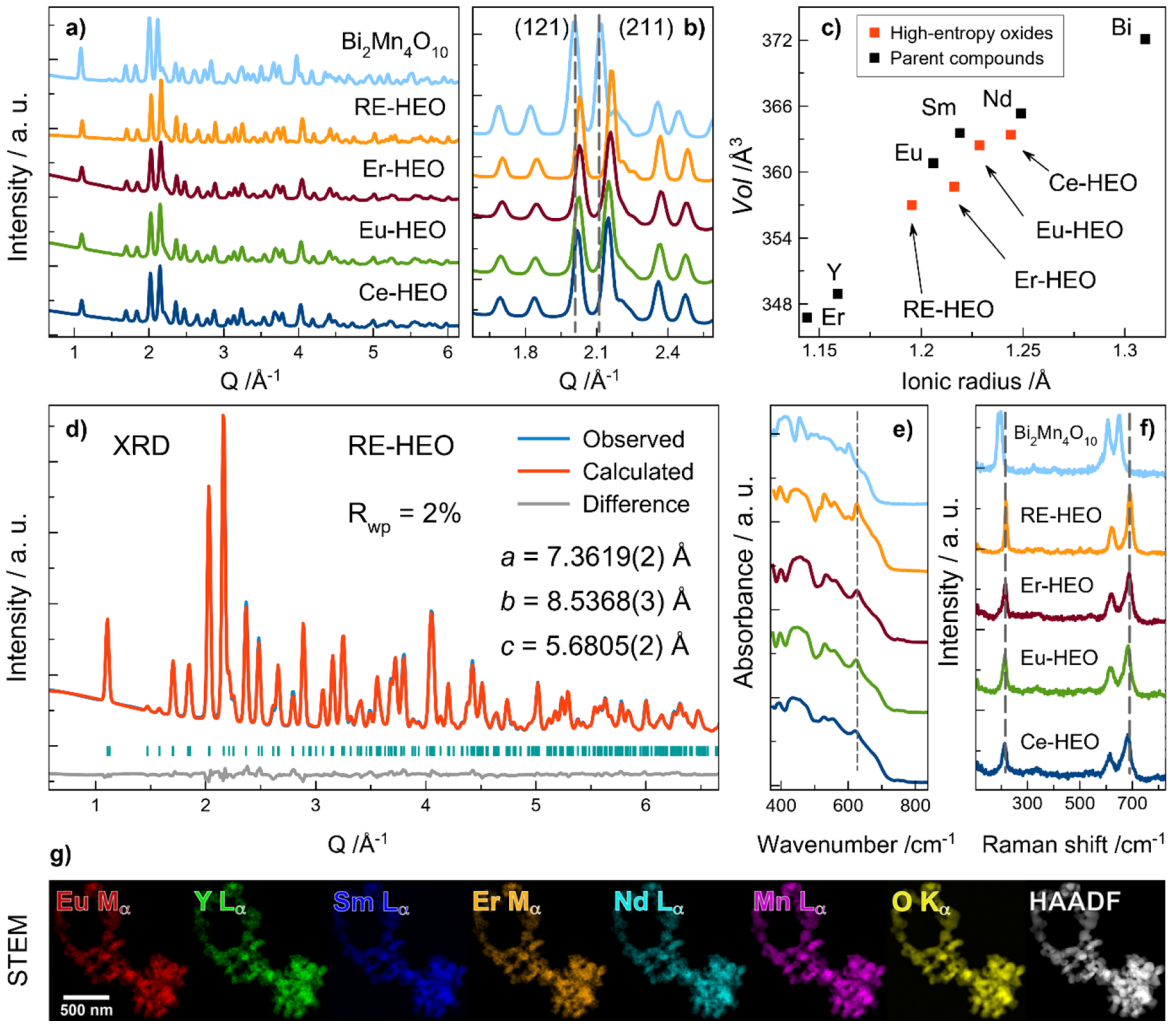

Figure 3. Structural characterization of $A_2Mn_4O_{10}$ (A = Nd, Sm, Y, Er, Eu, Ce, and Bi) high-entropy oxides. (a) Synchrotron X-ray diffraction patterns of RE-HEO, Er-HEO, Eu-HEO, and Ce-HEO in comparison with parent compound $Bi_2Mn_4O_{10}$. (b) The data show clear shifts of the (121) and (211) reflections. (c) Refined unit cell volume in dependence of ionic radii of the newly synthesized high-entropy oxides (red squares) and pure parent compounds[33,35,36] (black squares). (d) Rietveld refinement of synchrotron X-ray diffraction data of RE-HEO. (e) Infrared and (f) Raman spectra of $Bi_2Mn_4O_{10}$, RE-HEO, Er-HEO, Eu-HEO, and Ce-HEO. (g) STEM-EDX analysis of a representative particle of RE-HEO.

600 cm^{-1}, M-O stretching modes of MO_6 octahedra; 600−800 cm^{-1}, low-energy stretching vibrations of MO_4 tetrahedra and M−O−M bending vibrations of the double-tetrahedral units; and 800−900 cm^{-1}, high-energy stretching vibrations of MO_4 tetrahedra.[31] The latter are characteristic and distinguishable for the parent compounds, e.g., $Bi_2Fe_4O_9$; 812 cm^{-1},[31] $Bi_2Ga_4O_9$; 848 cm^{-1},[32] and $Bi_2Al_4O_9$; 922 cm^{-1} [31] (Figure 2c). In contrast, the IR spectrum of Bi-HEO shows very broad features in all three regions. Two seemingly broad bands with maxima at 850 and 888 cm^{-1} show up in the characteristic MO_4 stretching region, but a closer look reveals the overlap of several distinct peaks (Figure S8). Such a spectrum would be expected assuming a broad distribution of bond lengths and different combinations of vibrating oscillators in the double tetrahedral and/or pyramidal units. Considering only the M-O-M bending mode, we could expect 10 different combinations of oscillators in Bi-HEO, e.g., Mn−O−Mn, Fe−O−Fe, Al−O−Al, Ga−O−Ga, Ga−O−Al, Ga−O−Fe, Ga−O−Mn, Fe−O−Al, Fe−O−Mn, and Al−O−Mn. A clear band splitting in the IR spectra for $Bi_2Al_{4-x}Fe_xO_9$ solid solutions was also observed by Voll et al.[31]

While the IR spectrum of Bi-HEO mainly resembles the ones of the $Bi_2M_4O_9$ (M = Al, Ga, and Fe) parents, the Raman spectrum of Bi-HEO (Figure 2d) is quite similar to the one of $Bi_2Mn_4O_{10}$. However, compared to $Bi_2Mn_4O_{10}$, our HEO shows a significantly broader band distribution especially around the maxima at 608 and 644 cm^{-1}. In $Bi_2Mn_4O_{10}$, these bands are assigned to stretching modes of MnO_6 in the *ab*-plane and reported to be 605 and 647 cm^{-1}, respectively.[33] We assume that the broad distribution near these two mode frequencies in Bi-HEO arises due to local changes around the MnO_6 octahedra, significantly affecting its vibrational properties.

The elemental distribution of the various elements was mapped by STEM-EDX. The representative micrographs shown in Figure 2i and Figure S9 demonstrate that the particles have a broad size distribution ranging between ca. 100 and 2000 nm and contain all of the expected elements: Bi, Al, Fe, Ga, Mn, and O. Apart from well-mixed regions (Figure 2i and Figure S9a), some particles clearly show segregation (Figure S9b,c). Especially Al and Mn show some degree of anticorrelation, i.e., they prefer not to mix as can be seen in Figure S9c. Some particles show Ga-rich areas, which might be

https://doi.org/10.1021/acs.chemmater.3c01830
Chem. Mater. 2023, 35, 8664−8674

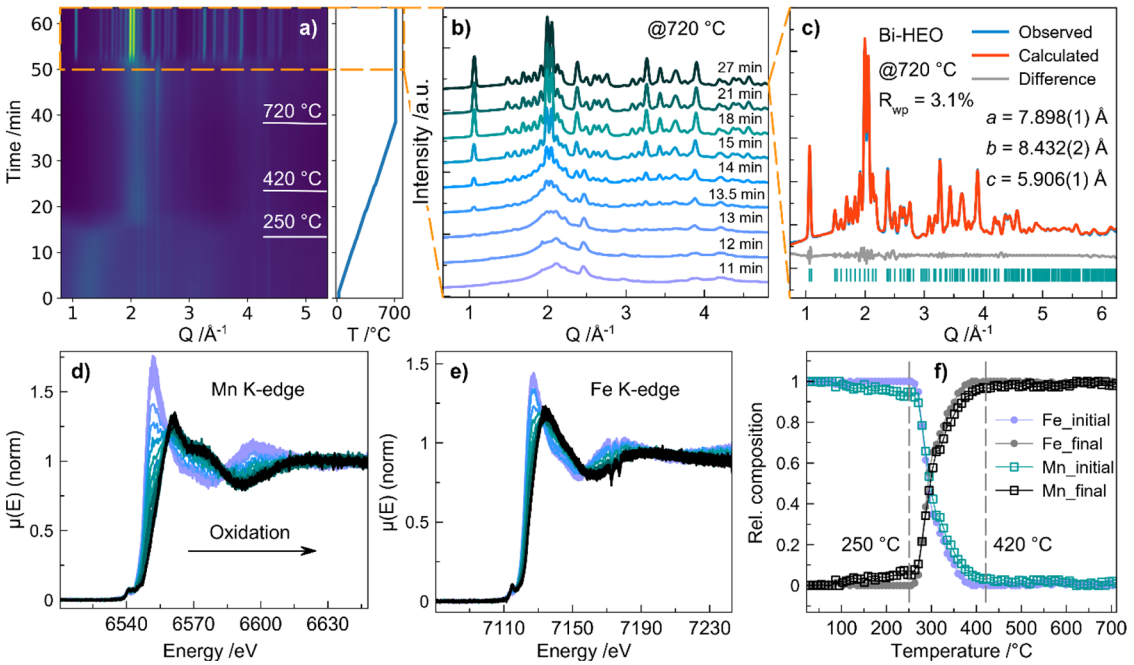

Figure 4. Formation of $Bi_2(Al_{0.25}Ga_{0.25}Fe_{0.25}Mn_{0.25})_4O_9$ (Bi-HEO). (a) Temperature-dependent X-ray diffraction patterns from room temperature to 720 °C and temperature profile. (b) Selected X-ray diffraction patterns collected at 720 °C. (c) Pawley refinement of a selected XRD pattern at 720 °C using the mullite structure in *Pbam* symmetry. Temperature-dependent XANES spectra collected at the (d) Mn K-edge and (e) Fe K-edge. (f) Linear component analysis using the initial and final states of the Mn and Fe XANES spectra.

related to the fact that Ga_2O_3 was used as the Ga source in the synthesis. This may lead to regions of higher heterogeneity due to slower reaction kinetics. Bi, Fe, and O seem to be well mixed in all particles. The observed heterogeneities could be small nanoparticles in the form of, e.g., binary oxides or hydroxides. Due to their low scattering power compared to Bi-containing compounds, such contributions would vanish in XRD, especially when the particles are small and in low concentration, e.g., in the range of 1−3%. This would be following the unexplained reflections observed in NPD, where Al (b = 3.449(5) barn)[34] and Ga (b = 7.288(2) barn)[34] impurities would be observable next to Bi (b = 8.532(2) barn),[34] Fe (b = 9.45(2) barn),[34] and Mn (b = −3.73(2) barn)[34] compounds due to their distinguishable coherent scattering lengths b. However, we expect these observed impurities to be minor phases in the material (<3%).

2.2. A-Site-Substituted $A_2Mn_4O_{10}$ High-Entropy Oxides. To further map out the synthetic accessibility of HEOs in the mullite-type system, we synthesized another four compounds, substituting the A-site of the $Bi_2Mn_4O_{10}$ parent (Figure 1b, overview of compounds in Figure 1f). Here, we chose lanthanides of various sizes, as well as Bi^{3+} and Y^{3+}. Three of the compounds contain Bi, and only one element (A) is exchanged A-HEO (A = Er, Eu, and Ce and HEO = Y, Sm, Nd, and Bi). The fourth compound RE-HEO, however, does not contain Bi, thus eliminating a possible influence of its stereoactive lone electron pair. Like Bi-HEO, the materials were synthesized by the sol−gel method. The phase purity and structure of the compounds were confirmed by synchrotron XRD (Figure 3a) and Rietveld refinements (Figures S10−S13, Table S3), shown for RE-HEO in Figure 3d. The data can be fitted with a structural model assuming a statistical distribution of the A-site cations and *Pbam* symmetry yielding R_{wp} values between 2 and 2.9%. With substitution, the reflections shift (Figure 3b). The refined unit cell parameters of the new HEOs are compared to the respective parent compounds $A_2Mn_4O_{10}$ (A = Er,[18] Y,[35] Eu,[36] Sm,[36] Nd,[37] and Bi) in Figure 3c (volume) and Figure S14 (*a*, *b*, and *c*). The values for $Ce_2Mn_4O_{10}$ are not given since this compound has not been reported so far, and our synthesis attempts were not successful. With the introduction of bigger ions into the crystal lattice, *a*, *b*, and *c* increase, as expected. The introduction of Bi^{3+} leads to a clear drop in *b* following the expected trends of the parent compounds (Figure S14b). The average crystallite sizes were refined to be 21(1)−37(2) nm for Er-HEO, Eu-HEO, and Ce-HEO and significantly bigger for RE-HEO with 221(17) nm, which was heated to a higher temperature (900 °C vs 700 °C). At the same time, the microstrain (ε_0) is an order of magnitude smaller (Table S3) than those in Er-HEO, Eu-HEO, and Ce-HEO, which might be related to the elimination of the stereochemically active lone electron pair of Bi in RE-HEO. The microstrain of all A-site-substituted HEOs, in general, is significantly smaller than the one determined for Bi-HEO (see Tables S1 and S3), and the reduction in correlation lengths in the PDFs is not observed (Figure S15). This is understandable considering the complex connectivity of substituted polyhedral sites in Bi-HEO compared to the substitution of lanthanides with close ionic radii in the A-site-substituted HEOs.

When comparing RE-HEO to $Bi_2Mn_4O_{10}$, the substitution of Bi^{3+} by RE^{3+} leads to strong shifts of vibrational frequencies in the IR (~25 cm^{-1}) and Raman spectra (~41 cm^{-1}), as can be seen in Figure 3e,f. This can be explained by structural changes involving the coordination polyhedra, e.g., bond lengths and polyhedral distortions, which these spectroscopy methods are very sensitive to.[38] We can follow the effect of the A-site substitution in our HEOs by the frequency shifts and induced peak broadening although the observable modes mainly involve the Mn coordinations.[33] As an example, the Raman spectrum of $Bi_2Mn_4O_{10}$ shows two signals at 187 and 199 cm^{-1}, whereas we observe only a single sharp feature at

https://doi.org/10.1021/acs.chemmater.3c01830
Chem. Mater. 2023, 35, 8664−8674

217 cm^{-1} for RE-HEO, which does not contain Bi. However, Er-HEO, Eu-HEO, and Ce-HEO, which contain Bi, also show broad asymmetric peak shoulders in that region. The same asymmetry can be observed in the higher energy region (~600 cm^{-1}), which we attribute to the influence of the Bi lone electron pair. In general, the spectral features observed for the A-site-substituted HEOs are significantly sharper than those for Bi-HEO, which highlights the large influence of the B-site substitution on the peak broadening (Figure 2d).

STEM-EDX analysis reveals a homogeneous distribution of the RE elements in the particles, as can be seen in Figure 3g (RE-HEO) and Figure S16 (other compositions). The materials possess an interesting open network structure of sintered nanoparticles with individual sizes of ca. 20 nm (Er-HEO, Eu-HEO, and Ce-HEO) and 150 nm (RE-HEO) matching the results of the Rietveld refinements (Table S3). The particles are highly crystalline (Figure S17e−h) as atomic column contrast can be observed in the high-resolution transmission micrographs (HRTEM) and Fast Fourier transformations (FFT) of selected areas (Figure S17, yellow squares) that clearly show sharp spots indicative of a highly ordered structure.

2.3. Formation of High-Entropy Mullite-Type Oxides. In contrast to most reports on the synthesis of HEOs, we use the sol−gel method instead of the classical solid-state approach. As described in detail in the Methods Section, metal nitrates are dissolved in stoichiometric amounts in diluted HNO_3 together with D-sorbitol, which is used as the complexing agent. From the solutions, a well-mixed precursor is thus produced, which is afterward calcined in air at 700 °C for 20 h. This temperature is sufficient for the HEOs to form, except for RE-HEO, which is heated to 900 °C for 20 h to yield the HEO product. This indicates that the use of Bi greatly promotes HEO crystallization, possibly due to its volatile nature at higher temperatures.[39]

To gain further insights into the crystallization mechanism, we followed the formation of the HEOs by in situ XRD and found that all compounds form through an amorphous intermediate without the formation of any crystalline phases, as seen in Figure 4a−c (Bi-HEO composition) and Figure S18 (other compositions). In all cases, the data show that the precursor is amorphous, except for Ga_2O_3, which is seen as a crystalline phase. The formation of the HEOs passes through two stages. First, the amorphous precursor transforms into a second amorphous phase of a different structure at ca. 300 °C, which then crystallizes directly into the respective HEO. The low temperature of the first transition indicates that the precursor powder consists of components containing nitrates/organics as these have typical decomposition temperatures in this temperature range. The transformation of the amorphous precursor into the amorphous intermediate is accompanied by a drastic change in position of the main scattering from ~1.3 to ~2.2 $Å^{-1}$ (see Figure 4a). The increase in the scattering angle implies that a larger phase transforms into a smaller one, which fits into the picture of a decomposing phase through the loss of its contained organic components. In the case of Bi-HEO, the Bragg peaks from Ga_2O_3 disappear when the mullite-type structure forms. While Bi-HEO needs a reaction time of about 14 min at 720 °C (52 min in total) to form, Er-HEO, Eu-HEO, and Ce-HEO start to crystallize already at 670 °C. The first reflections of RE-HEO can be observed after 22 min at 720 °C (60 min in total); however, even after 100 min at 720 °C (140 min in total), the intermediate phase did not completely convert into the mullite-type structure (Figure S18d). In addition, we followed the changes in the oxidation states of Mn and Fe during the formation of Bi-HEO via X-ray absorption spectroscopy (XAS) (Figure 4d−f). Both Mn and Fe oxidize between ca. 250 and 420 °C as determined by linear component analysis and demonstrated in Figure 4f. Remarkably, they oxidize exactly at the same time, as the curves of both species almost overlay (Figure 4f). Thereafter, no significant change can be observed, suggesting that the transition of the precursor into the amorphous intermediate lays the foundation for the later crystallization of the final products. Of note, the crystallization of Bi-HEO in the coupled XAS/XRD experiments is observed at ca. 640 °C (Figure S19) compared to 720 °C in the XRD experiments (Figure 4a). This can be explained by the significant difference in heating rates (XAS/XRD = 1.7 K min^{-1}; XRD = 20 K min^{-1}) likely changing the kinetics of the crystallization process. To follow the structural changes during the phase formation of the HEOs in more detail, we performed sequential Rietveld refinements on the diffraction patterns collected at 720 °C. For all materials, we observe a reduction of unit cell volume during growth, as presented in Figure S20c. This surprising result is in line with earlier studies on $Bi_2Fe_4O_9$[40] and suggests that this volume contraction is a general phenomenon during the growth of mullite-type compounds as it seems to be independent of chemical composition. The crystallites of the A-site-substituted HEOs grow very sluggishly, as can be seen in Figure S20b. We have fitted the crystallite growth curves using a saturation growth rate equation of the form

$$y = a\frac{x - c}{b + (x - c)} \quad (1)$$

with fitting parameters a, b, and c. Here, a represents the saturation crystallite size, whereas c can be seen as the starting point of the crystal growth. The predicted saturation sizes by the fitted model and the refined crystallite sizes of the heated HEOs (700 °C for 20 h) show excellent agreement, as can be seen in Table S4. As an example, for Ce-HEO, we observe a crystallite size of 35(1) nm after heating at 700 °C for 20 h compared to a predicted size by the model of 30.3(1) nm. We take this result as a confirmation that the crystal growth of our calcined HEOs have reached saturation in the nanoregime although calcination at high temperatures. This observation is surprising and offers the possibility to control the sizes of the crystallites solely through the adjustment of calcination temperature. In a broader context, synthesizing a material in a high-entropy version might be a route to produce nanomaterials of structures usually only accessible at high temperatures. The combination of the sluggish crystal growth and the saturation growth behavior in the nanoregime suggests that the chemical gradients in the material are very small, i.e., the precursor is highly homogeneous. The high homogeneity combined with the high number of different chemical constituents may lead to a slow atomic diffusion rate due to low chemical potentials. From the local perspective of an atom, the surrounding potential might not differ much, and as such, material diffusion might be inhibited. As soon as the temperature is high enough, the material crystallizes very suddenly, and many grains are formed at the same time. This in turn could explain the lack of Ostwald ripening as all crystallites would be of ca. the same size. However, this hypothesis is of speculative nature. The exact mechanism of the sluggish growth behavior is out of the scope of this paper

https://doi.org/10.1021/acs.chemmater.3c01830
Chem. Mater. 2023, 35, 8664−8674

and will need further evaluation. To investigate if any impurities would form upon cooling, we continued to collect data in the XRD experiments after the HEOs had formed at 720 °C and the heating process was stopped. None of the $A_2Mn_4O_{10}$ HEOs show any phase separation as can be seen in Figure S21. For Bi-HEO, however, we observe the appearance of new reflections (Figure S22) during cooling. While the pattern at 720 °C can be described excellently with the *Pbam* lattice symmetry (Figure 4c), the patterns below 690 °C clearly cannot. This led us to repeat the synthesis several times, and although every synthesis attempt showed the formation of Bi-HEO as the main phase, the formation of this impurity phase was regularly observed in varying amounts (see Figure S23). We identified this phase as sillenite-type $Bi_{25}GaO_{39}$,[41] which can be dissolved by diluted HNO_3 (Figure S23, inset). The formation of $Bi_{25}GaO_{39}$ may be related to the insolubility of Ga_2O_3 in the precursor mixture leading to Ga-rich regions in the material (see the section on B-Site-Substituted $Bi_2(Al_{0.25}Fe_{0.25}Ga_{0.25}Mn_{0.25})_4O_9$).

3. CONCLUSIONS

With this work, we report the first successful synthesis of HEOs in a mullite-type structure and thereby introduce a completely new family for the design of HEOs with potentially exciting properties. To demonstrate the wide accessible compound space, we present five samples with varying compositions spanning different ionic sizes. Applying the HE concept to mullite-type materials offers a tremendous platform to study and tune a diversity of desired functional properties by exchange of either the A- or B-sites of these compounds. As an example, we demonstrate a change of magnetic behavior for B-site-substituted Bi-HEO using NPD. Further investigations of the magnetic properties and structures of $A_2Mn_4O_{10}$ HEOs hold great potential for new discoveries.

We revealed the wide synthetic accessibility of only two compounds in the mullite-type family. However, the compound space is immense, and we expect that the synthesis of other HEOs of this family is possible including, e.g., $RECrGeO_5$,[42] $REAlGeO_5$,[43] $REFeMnO_5$,[44] and $RECrMnO_5$.[45] As such, we created a potentially large space of interesting new HEOs, which are worth exploring toward a variety of applications.

All compounds studied here crystallize via a two-step process. First, the amorphous precursor transforms into an amorphous phase with a different structure, from which the HEOs crystallize directly without the formation of any crystalline oxides as intermediates, proving that the homogeneity is maintained throughout the synthesis. This observation is surprising as thermodynamically stable compounds are known to exist in this temperature regime, e.g., several polymorphs of manganese oxide. This let us conclude that the pathway through the intermediate amorphous phase allows bypassing possible thermodynamic wells in the energy landscape of formation enthalpy. This might explain why there are so few HEO structure-types known so far as the traditional solid-state route has mainly been used for their synthesis. We expect that the presented synthesis is very effective also in the fabrication of HEOs of other structure types, and many reports of new materials with interesting properties will follow.

4. METHODS

4.1. Syntheses. Syntheses were performed by using the sol−gel method. First, an acidic solution with 26 mL of deionized H_2O, 3 mL of conc. HNO_3 (TraceSELECT for trace analysis, >69.0, Honeywell), and 1.29 g of D-sorbitol (≥98%, Sigma-Aldrich) is produced. After that, a total of 7.5 mmol of the respective metal nitrates in the given stoichiometry is dissolved. Heating the solution at 90 °C in a glycerine bath for 2 h leads to a gel, which is subsequently heated in air at 250 °C for 18 h in an oven to obtain a solid "foam" precursor. This precursor is afterward ground and calcined in a porcelain crucible in air at 700 °C for 20 h (900 °C for 20 h; RE-HEO) to form the nanocrystalline products. We did not observe any reaction of the materials with the porcelain crucible under the given conditions. All educts were of analytical grade and used as received: bismuth(III) nitrate pentahydrate (ACS reagent, ≥98.0%, Sigma-Aldrich), aluminum(III) nitrate nonahydrate (ACS reagent, ≥98%, Sigma-Aldrich), gallium(III) oxide (99.99+% metals basis, Sigma-Aldrich), manganese(II) nitrate tetrahydrate (purum p.a., ≥ 97.0% (KT), Sigma-Aldrich), iron(III) nitrate nonahydrate (ACS reagent, ≥98%, Sigma-Aldrich), europium(III) nitrate hydrate (99.99% trace metals basis, Sigma-Aldrich), yttrium(III) nitrate hexahydrate, (99.9% Y, abcr), samarium(III) nitrate hexahydrate (99.9% trace metals basis, Sigma-Aldrich), neodymium(III) nitrate hexahydrate (99.9% trace metals basis, Sigma-Aldrich), erbium(III) nitrate pentahydrate (99.9% trace metals basis, Sigma-Aldrich), and ammonium cerium(IV) nitrate (for analysis EMSURE ACS, Reag. Ph Eur, Sigma-Aldrich).

4.2. Structural Characterization. Room temperature X-ray diffraction and total scattering data were collected at P02.1 at the PETRA III/DESY in Hamburg, Germany. Measurements have been carried out on samples in 1 mm Kapton capillaries using a wavelength of 0.20741 Å and a PerkinElmer XRD1621 CN3 area detector with a sample detector distance of about 600 mm (XRD, center geometry) and about 270 mm (PDF, corner geometry). The exposure times were 60 and 300 s for XRD and PDF measurements. Data were integrated using pyFAI[46] and the PDFs obtained using xPDFSuite[47] with a Qmax and rPoly of 21.5 $Å^{-1}$ and 0.9, respectively. The scattering pattern of an empty Kapton capillary was used for background subtraction.

In situ X-ray diffraction data were collected at P21.1 at PETRA III/DESY in Hamburg, Germany using a wavelength of 0.1220319 Å and a PerkinElmer XRD1621 area detector with a sample detector distance of ca. 500 mm RE-HEO and 1500 mm (all other compositions). The powder samples were placed in an open quartz capillary in the horizontal position. The capillary was only half filled and left open at one end to allow for gas exchange. The temperature was increased using a heating fan and a heating rate of 20 K min^{-1}. For the crystallization experiments, the samples were heated from room temperature to 720 °C and kept there for ca. 2 h. After that, the samples were cooled naturally while the XRD patterns were still collected. In the heating/cooling experiments on crystalline $Bi_2(Al_{0.25}Fe_{0.25}Ga_{0.25}Mn_{0.25})_4O_9$, the sample was heated from room temperature to 720 °C and cooled back to room temperature with a ramp of 20 K min^{-1}. The procedure was performed twice in total.

Neutron powder diffraction data on a $Bi_2(Al_{0.25}Fe_{0.25}Ga_{0.25}Mn_{0.25})_4O_9$ compound were collected with a high-resolution powder neutron diffractometer HRPT at the SINQ Spallation Neutron Source at PSI, Switzerland.[48] The instrument was used in high intensity mode and with the neutron wavelength 1.8857 Å. A sample was closed in a vanadium container, and the data were collected at 1.7 and 300 K. The NPD data of $Bi_2Fe_4O_9$ were collected on samples at 100 and 300 K on the NOMAD instrument,[49] at the Spallation Neutron Source (SNS) at Oak Ridge National Laboratory, Tennessee, USA.

Refinements of XRD, PDF, and NPD data were performed using Topas Academic.[50] The instrumental resolution functions (IRF) were determined by fitting against standards of LaB_6 (room temperature XRD and PDF, P02.1), Ni (in situ XRD, P21.1), and $Na_2Ca_3Al_2F_{14}$ (NPD, HRPT). XRD and NPD data were fitted by the Pawley[51] and Rietveld method.[52] Rietveld and PDF refinements of the X-ray data

https://doi.org/10.1021/acs.chemmater.3c01830
Chem. Mater. 2023, 35, 8664−8674

were performed by using a model with a statistical distribution of the nominal compositions over the respective crystallographic sites. Refined parameters (Table S1) are the scale factor, lattice parameters, atomic displacement parameters (ADP), atomic coordinates, one Lorentzian profile parameter to calculate *LVol-IB* for the apparent average crystallite size, and one Gaussian profile parameter for calculating ε_0 as the microstrain. In the refinements of the NPD data, the occupancy of the individual elements was refined on the 4e and 4h sites, however constrained to the weighted nominal composition and alternatingly with the respective ADPs. The temperature-dependent XRD data of the crystallized Bi-HEO was refined sequentially using the Pawley method. The time-dependent XRD data collected at 720 °C during the formation of Bi-HEO, Eu-HEO, Ce-HEO, and Er-HEO was refined using the Rietveld method. We performed sequential refinements starting from the last pattern of the most crystalline sample and going backward toward the least crystalline sample. The resulting crystal growth curves for Eu-HEO, Er-HEO, and CE-HEO were fitted using a saturation growth rate equation of the form $y = a((x - c)/b + (x - c))$ (eq 1) with fitting parameters *a*, *b*, and *c*. The PDFs were refined in the ranges 1−60, 1−25, and 25−60 Å. Refined parameters were the scale factor, lattice parameters, atomic displacement parameters (ADP), atomic coordinates, and sp-diameter. The PDFs of the "simulated physical mixtures" were calculated by PDFgui[53] using the experimental instrumental parameters and assuming each 1/4 for $Bi_2(Al_{0.25}Fe_{0.25}Ga_{0.25}Mn_{0.25})_4O_9$ of the total scaling factor for the respective parent compounds.

4.3. Spectroscopy. Raman spectra were measured on an inVia Qontor confocal Raman microscope using the Wire v. 5.4 software (Renishaw, Gloucestershire, UK) with a CCD detector. A laser excitation of 785 nm (yellow laser), laser power of 10 mW, dispersed by a 1200 lines mm^{-1} grating, and exposition for 10 s and 10 accumulations were used for $Bi_2(Al_{0.25}Fe_{0.25}Ga_{0.25}Mn_{0.25})_4O_9$, $Bi_2Al_4O_9$, $Bi_2Ga_4O_9$, $Bi_2Fe_4O_9$, and $Bi_2Mn_4O_{10}$. Data for the A-site-substituted $A_2Mn_4O_{10}$ HEOs were collected using a laser excitation of 532 nm (green laser), laser power of 5 mW, dispersed by a 1800 lines mm^{-1} grating, and exposition for 100 s and 5 accumulations. Data were collected between 100 and 3200 cm^{-1}.

Infrared spectra were measured with 64 scans from 374 to 4000 cm^{-1} using a Bruker Alpha P FT IR spectrometer in attenuated total reflectance (ATR) detection.

Coupled in situ XRD and XAS data were collected at Swiss Norwegian Beamline (SNBL) BM31, ESRF, Grenoble. The solid precursors were placed with quartz wool plugs in both side open-ended quartz capillaries (0.8 mm diameter). The capillary was glued into an in situ flow-through reactor available at the beamline that was connected to gas lines by Swagelok connections.[54,55] Synthetic air was flowed through the capillary with a flow rate of 5 mL min^{-1}. The capillary was heated with a gas blower at a constant heating ramp of 1.7 K min^{-1}, while XRD and XAS data were collected consecutively. XAS-XRD data were collected in a quasi-simultaneous manner using a Si(111) double crystal monochromator (DCM). XANES spectra were acquired at the Fe K-edege (7112 eV) and Mn K-edge (6539 eV) in fluorescence mode with a Vortex one-element silicon drift detector (SDD) and FalconX electronics for extremely high count rate performance. In situ X-ray diffraction data were collected with a wavelength of 0.338591 Å, using a 2D DEXELA CMOS (complementary metal-oxide semiconductor) pixel detector with a sample detector distance of ca. 420 mm.

XANES spectra were treated with the ATHENA[56] and LARCH program package.[57] The linear combination analysis (LCA) was performed with LARCH using the initial precursor spectra and the final oxide spectra as the respective components for the LCA fits.

4.4. Electron Microscopy and STEM-EDX Analysis. The nanoparticle (NP) samples were suspended in ethanol and subsequently drop-casted onto Cu 300 mesh grids with 2 nm carbon (Quantifoil). High-resolution transmission electron microscopy (HR-TEM) images were collected on an FEI Talos FX-200 equipped with a Ceta 16 M camera with samples mounted in a double tilt holder. The FIJI software was used to crop out quadratic regions of interest around selected NPs oriented with their major zone axes aligned with the optical axis.[58] These smaller cropped regions were apodized using a Hann window and, subsequently, fast Fourier transformed (FFT) using HyperSpy.[59] The resulting power spectra of the FFT images are displayed on a log scale with the minimum value set to display the 30th percentile. Scanning transmission electron microscopy (STEM) images were collected by using the same electron microscope in STEM mode and by using a 10.5 mrad converged electron probe. The collection angle of the STEM high-angle annular dark-field (HAADF) images was 60−200 mrad. STEM energy-dispersive X-ray spectroscopy (EDX) data sets were collected using the ChemiSTEM Gen1 system installed on the Talos Microscope. Data analysis and plotting were subsequently performed using HyperSpy and FIJI. Specifically, the elemental distribution maps presented in the manuscript are produced by using HyperSpy to rebin the collected data spatially to increase signal-to-noise ratio and subsequently subtract background counts by performing linear interpolation around the relevant elemental lines. Finally, the color maps representing the spatial distribution of different elements shown in the manuscript are produced by using FIJI.

■ ASSOCIATED CONTENT

Data Availability Statement

All relevant data within the article are available from the corresponding authors on reasonable request.

Supporting Information

The Supporting Information is available free of charge at https://pubs.acs.org/doi/10.1021/acs.chemmater.3c01830.

Rietveld and Pawley refinements of synchrotron X-ray diffraction data from all compounds including the results in a tabulated form; temperature-dependent lattice parameters of Bi-HEO; Pawley refinement of neutron diffraction data for Bi-HEO; pair distribution functions of all synthesized HEOs and parent compounds $Bi_2M_4O_9$ (M = Fe, Ga, and Al) and $Bi_2Mn_4O_{10}$; PDF refinements of Bi-HEO; Gaussian fits of FTIR data; comparison of lattice parameters from synthesized HEOs and parent compounds; STEM-EDX and HAADF images of the synthesized HEOs; in situ diffraction data of the formation of the HEOs; crystallite size growth curves along with volume evolution during the formation of the HEOs; comparison between XRD patterns of products formed during the in situ heating experiments and after cooling; reproducibility test of Bi-HEO (PDF)

■ AUTHOR INFORMATION

Corresponding Authors

Andrea Kirsch − *Department of Chemistry and Nanoscience Center, University of Copenhagen, Copenhagen 2100, Denmark;* orcid.org/0000-0003-2602-7415; Email: anki@chem.ku.dk

Kirsten M. Ø. Jensen − *Department of Chemistry and Nanoscience Center, University of Copenhagen, Copenhagen 2100, Denmark;* orcid.org/0000-0003-0291-217X; Email: kirsten@chem.ku.dk

Authors

Espen Drath Bøjesen − *Interdisciplinary Nanoscience Center & Aarhus University Centre for Integrated Materials Research, Aarhus University, Aarhus 8000, Denmark;* orcid.org/0000-0002-9352-9514

Niels Lefeld − *Institute of Inorganic Chemistry and Crystallography, University of Bremen, Bremen 28359, Germany*

https://doi.org/10.1021/acs.chemmater.3c01830
Chem. Mater. 2023, 35, 8664−8674

Rasmus Larsen − *Interdisciplinary Nanoscience Center & Aarhus University Centre for Integrated Materials Research, Aarhus University, Aarhus 8000, Denmark*

Jette Katja Mathiesen − *Department of Chemistry and Nanoscience Center, University of Copenhagen, Copenhagen 2100, Denmark; Department of Physics, Technical University of Denmark, Kgs. Lyngby DK-2800, Denmark*

Susanne Linn Skjærvø − *Department of Chemistry and Nanoscience Center, University of Copenhagen, Copenhagen 2100, Denmark*

Rebecca Katharina Pittkowski − *Department of Chemistry and Nanoscience Center, University of Copenhagen, Copenhagen 2100, Denmark;* orcid.org/0000-0002-0351-4993

Denis Sheptyakov − *Laboratory for Neutron Scattering and Imaging, Paul Scherrer Institut, Villigen 5232, Switzerland*

Complete contact information is available at: https://pubs.acs.org/10.1021/acs.chemmater.3c01830

Author Contributions

A.K. and K.M.Ø.J. planned the project. A.K. designed, synthesized, characterized (Raman and IR) the compounds, and analyzed the Raman, IR, XRD, PDF, and NPD data. A.K., N.L., J.K.M., and S.L.S. acquired the in situ XRD data at beamline P21.1. N.L. helped with data visualization. E.D.B. acquired and analyzed the TEM data with the help of R.L. D.S. acquired the NPD data at PSI, HRPT, Switzerland. R.K.P. acquired and analyzed the XANES data. The manuscript was written by A.K. and revised by K.M.Ø.J. with the help of all other authors.

Notes

The authors declare no competing financial interest.

■ ACKNOWLEDGMENTS

This work is part of a project that has received funding from the European Research Council (ERC) under the European Union's Horizon 2020 Research and Innovation Programme (grant agreement no. 804066). We are grateful to the Villum Foundation for financial support through a Villum Young Investigator grant (VKR00015416). J.K.M. acknowledges funding from VILLUM FONDEN, research grant (41388). Funding from the Danish Ministry of Higher Education and Science through the SMART Lighthouse is gratefully acknowledged. We acknowledge support from the Danish National Research Foundation Center for High-Entropy Alloy Catalysis (DNRF 149). The Danish Research Council is acknowledged for covering travel expenses in relation to the synchrotron experiment (DanScatt). A.K. gratefully acknowledges the Deutsche Forschungsgemeinschaft (DFG, German science foundation) for funding of the project Ki 2427/1-1 (# 429360100). We acknowledge DESY (Hamburg, Germany), a member of the Helmholtz Association HGF, for the provision of experimental facilities. Parts of this research were carried out at PETRA III beamlines P02.1 and P21.1. We would like to thank Dr. Soham Banerjee for assistance in using beamline P21.1 and Dr. Martin Etter and Dr. Alexander Schökel for assistance in using beamline P02.1. Beamtime was allocated for proposals I-20200547 and I-20210486 EC. A portion of this research used resources at the Spallation Neutron Source, a DOE Office of Science User Facility operated by the Oak Ridge National Laboratory. We thank Dr. Jue Liu for collecting data at beamline NOMAD. Beamtime was allocated for proposal IPTS-24814. This work is partly based on experiments performed at the Swiss spallation neutron source SINQ, Paul Scherrer Institute, Villigen, Switzerland. We acknowledge the European Synchrotron Radiation Facility for provision of synchrotron radiation facilities, and we would like to thank Dr. Dragos Stoian for assistance in using beamline BM31 (SNBL). We acknowledge Assoc. Prof. Heloisa Bordallo and Dr. Mathias Dowds from University of Copenhagen, Denmark, for assistance in collecting Raman and infrared spectra. The Raman microscope used in this work was financed by the Carlsberg grant CF19-0521.

■ REFERENCES

(1) Yeh, J.-W.; Chen, S.-K.; Lin, S.-J.; Gan, J.-Y.; Chin, T.-S.; Shun, T.-T.; Tsau, C.-H.; Chang, S.-Y. Nanostructured High-Entropy Alloys with Multiple Principal Elements: Novel Alloy Design Concepts and Outcomes. *Adv. Eng. Mater.* **2004**, *6* (5), 299−303.

(2) Huang, P.-K.; Yeh, J.-W.; Shun, T.-T.; Chen, S.-K. Multi-Principal-Element Alloys with Improved Oxidation and Wear Resistance for Thermal Spray Coating. *Adv. Eng. Mater.* **2004**, *6* (12), 74−78.

(3) McCormack, S. J.; Navrotsky, A. Thermodynamics of High Entropy Oxides. *Acta Mater.* **2021**, *202*, 1−21.

(4) Rost, C. M.; Sachet, E.; Borman, T.; Moballegh, A.; Dickey, E. C.; Hou, D.; Jones, J. L.; Curtarolo, S.; Maria, J.-P. Entropy-Stabilized Oxides. *Nat. Commun.* **2015**, *6* (1), 8485.

(5) Banerjee, R.; Chatterjee, S.; Ranjan, M.; Bhattacharya, T.; Mukherjee, S.; Jana, S. S.; Dwivedi, A.; Maiti, T. High-Entropy Perovskites: An Emergent Class of Oxide Thermoelectrics with Ultralow Thermal Conductivity. *ACS Sustain. Chem. Eng.* **2020**, *8* (46), 17022−17032.

(6) Bérardan, D.; Franger, S.; Meena, A. K.; Dragoe, N. Room Temperature Lithium Superionic Conductivity in High Entropy Oxides. *J. Mater. Chem. A* **2016**, *4* (24), 9536−9541.

(7) Sarkar, A.; Eggert, B.; Velasco, L.; Mu, X.; Lill, J.; Ollefs, K.; Bhattacharya, S. S.; Wende, H.; Kruk, R.; Brand, R. A.; Hahn, H. Role of Intermediate 4 f States in Tuning the Band Structure of High Entropy Oxides. *APL Mater.* **2020**, *8* (5), No. 051111.

(8) Oses, C.; Toher, C.; Curtarolo, S. High-Entropy Ceramics. *Nat. Rev. Mater.* **2020**, *5* (4), 295−309.

(9) Witte, R.; Sarkar, A.; Kruk, R.; Eggert, B.; Brand, R. A.; Wende, H.; Hahn, H. High-Entropy Oxides: An Emerging Prospect for Magnetic Rare-Earth Transition Metal Perovskites. *Phys. Rev. Mater.* **2019**, *3* (3), No. 034406.

(10) Djenadic, R.; Sarkar, A.; Clemens, O.; Loho, C.; Botros, M.; Chakravadhanula, V. S. K.; Kübel, C.; Bhattacharya, S. S.; Gandhi, A. S.; Hahn, H. Multicomponent Equiatomic Rare Earth Oxides. *Mater. Res. Lett.* **2017**, *5* (2), 102−109.

(11) Parida, T.; Karati, A.; Guruvidyathri, K.; Murty, B. S.; Markandeyulu, G. Novel Rare-Earth and Transition Metal-Based Entropy Stabilized Oxides with Spinel Structure. *Scr. Mater.* **2020**, *178*, 513−517.

(12) Jiang, B.; Bridges, C. A.; Unocic, R. R.; Pitike, K. C.; Cooper, V. R.; Zhang, Y.; Lin, D.-Y.; Page, K. Probing the Local Site Disorder and Distortion in Pyrochlore High-Entropy Oxides. *J. Am. Chem. Soc.* **2021**, *143* (11), 4193−4204.

(13) Simonov, A.; Goodwin, A. L. Designing Disorder into Crystalline Materials. *Nat. Rev. Chem.* **2020**, *4* (12), 657−673.

(14) Singh, A. K.; Kaushik, S. D.; Kumar, B.; Mishra, P. K.; Venimadhav, A.; Siruguri, V.; Patnaik, S. Substantial Magnetoelectric Coupling near Room Temperature in Bi2Fe4O9. *Appl. Phys. Lett.* **2008**, *92* (13), 132910.

(15) Chattopadhyay, S.; Petit, S.; Ressouche, E.; Raymond, S.; Balédent, V.; Yahia, G.; Peng, W.; Robert, J.; Lepetit, M.-B.; Greenblatt, M.; Foury-Leylekian, P. 3d-4f Coupling and Multi-ferroicity in Frustrated Cairo Pentagonal Oxide DyMn2O5. *Sci. Rep.* **2017**, *7* (1), 14506.

(16) Zheng, Y.; Thampy, S.; Ashburn, N.; Dillon, S.; Wang, L.; Jangjou, Y.; Tan, K.; Kong, F.; Nie, Y.; Kim, M. J.; Epling, W. S.; Chabal, Y. J.; Hsu, J. W. P.; Cho, K. Stable and Active Oxidation Catalysis by Cooperative Lattice Oxygen Redox on SmMn2O5Mullite Surface. *J. Am. Chem. Soc.* **2019**, *141* (27), 10722−10728.
(17) Ressouche, E.; Simonet, V.; Canals, B.; Gospodinov, M.; Skumryev, V. Magnetic Frustration in an Iron-Based Cairo Pentagonal Lattice. *Phys. Rev. Lett.* **2009**, *103* (26), No. 267204.
(18) Alonso, J. A.; Casais, M. T.; Martínez-Lope, M. J.; Martínez, J. L.; Fernández-Díaz, M. T. A Structural Study from Neutron Diffraction Data and Magnetic Properties of RMn2O5 (R = La, Rare Earth). *J. Phys.: Condens. Matter* **1997**, *9* (40), 8515−8526.
(19) Noda, Y.; Kimura, H.; Fukunaga, M.; Kobayashi, S.; Kagomiya, I.; Kohn, K. Magnetic and Ferroelectric Properties of Multiferroic RMn2O5. *J. Phys.: Condens. Matter* **2008**, *20* (43), No. 434206.
(20) Johnstone, G. H. J.; González-Rivas, M. U.; Taddei, K. M.; Sutarto, R.; Sawatzky, G. A.; Green, R. J.; Oudah, M.; Hallas, A. M. Entropy Engineering and Tunable Magnetic Order in the Spinel High-Entropy Oxide. *J. Am. Chem. Soc.* **2022**, *144* (45), 20590−20600.
(21) Mazza, A. R.; Skoropata, E.; Sharma, Y.; Lapano, J.; Heitmann, T. W.; Musico, B. L.; Keppens, V.; Gai, Z.; Freeland, J. W.; Charlton, T. R.; Brahlek, M.; Moreo, A.; Dagotto, E.; Ward, T. Z. Designing Magnetism in High Entropy Oxides. *Adv. Sci.* **2022**, *9* (10), 2200391.
(22) Batchelor, T. A. A.; Pedersen, J. K.; Winther, S. H.; Castelli, I. E.; Jacobsen, K. W.; Rossmeisl, J. High-Entropy Alloys as a Discovery Platform for Electrocatalysis. *Joule* **2019**, *3* (3), 834−845.
(23) Löffler, T.; Ludwig, A.; Rossmeisl, J.; Schuhmann, W. What Makes High-Entropy Alloys Exceptional Electrocatalysts? *Angew. Chem., Int. Ed.* **2021**, *60* (52), 26894−26903.
(24) Kirsch, A.; Murshed, M. M.; Schowalter, M.; Rosenauer, A.; Gesing, T. M. Nanoparticle Precursor into Polycrystalline Bi2Fe4O9: An Evolutionary Investigation of Structural, Morphological, Optical, and Vibrational Properties. *J. Phys. Chem. C* **2016**, *120* (33), 18831−18840.
(25) Selbach, S. M.; Einarsrud, M.-A.; Grande, T. On the Thermodynamic Stability of BiFeO3. *Chem. Mater.* **2009**, *21* (1), 169−173.
(26) Jiang, B.; Yu, Y.; Cui, J.; Liu, X.; Xie, L.; Liao, J.; Zhang, Q.; Huang, Y.; Ning, S.; Jia, B.; Zhu, B.; Bai, S.; Chen, L.; Pennycook, S. J.; He, J. High-Entropy-Stabilized Chalcogenides with High Thermoelectric Performance. *Science* **2021**, *371* (6531), 830−834.
(27) Philippot, G.; Boejesen, E. D.; Elissalde, C.; Maglione, M.; Aymonier, C.; Iversen, B. B. Insights into $BaTi_{1-y}Zr_yO_3$ ($0 \leq y \leq 1$) Synthesis under Supercritical Fluid Conditions. *Chem. Mater.* **2016**, *28* (10), 3391−3400.
(28) Shannon, R. D. Revised Effective Ionic Radii and Systematic Studies of Interatomie Distances in Halides and Chalcogenides. *Acta Crystallogr.* **1976**, *A32*, 751−767.
(29) Muñoz, A.; Alonso, J. A.; Casais, M. T.; Martínez-Lope, M. J.; Martínez, J. L.; Fernández-Díaz, M. T. Magnetic Structure and Properties of BiMn2O5 Oxide: A Neutron Diffraction Study. *Phys. Rev. B* **2002**, *65* (14), No. 144423.
(30) Singh, A. K.; Mohapatra, S. R.; Khare, P.; Ganguli, N.; Wildes, A.; Siruguri, V.; Kaushik, S. D. Neutron Diffraction and Short Range Ordering Study in Multiferroic Bi2Fe4O9. *Mater. Res. Express* **2019**, *6* (6), No. 066107.
(31) Voll, D.; Beran, A.; Schneider, H. Variation of Infrared Absorption Spectra in the System Bi2Al4−xFexO9 (x = 0−4), Structurally Related to Mullite. *Phys. Chem. Miner.* **2006**, *33* (8−9), 623−628.
(32) Beran, A.; Libowitzky, E.; Burianek, M.; Mühlberg, M.; Pecharromán, C.; Schneider, H. Infrared and Raman Spectroscopy of Mullite-Type Bi2Ga4O9. *Cryst. Res. Technol.* **2008**, *43* (11), 1230−1239.
(33) Silva Júnior, F. M.; Paschoal, C. W. A.; Almeida, R. M.; Moreira, R. L.; Paraguassu, W.; Castro Junior, M. C.; Ayala, A. P.; Kann, Z. R.; Lufaso, M. W. Room-Temperature Vibrational Properties of the BiMn2O5Mullite. *Vib. Spectrosc.* **2013**, *66*, 43−49.
(34) Sears, V. F. Neutron Scattering Lengths and Cross Sections. *Neutron News* **1992**, *3* (3), 26−37.
(35) de la Calle, C.; Alonso, J. A.; Martínez-Lope, M. J.; García-Hernández, M.; André, G. Synthesis under High-Oxygen Pressure, Magnetic and Structural Characterization from Neutron Powder Diffraction Data of YGa1−xMn1+xO5 (X = 0.23): A Comparison with YMn2O5. *Mater. Res. Bull.* **2008**, *43* (2), 197−206.
(36) Alonso, J. A.; Casais, M. T.; Martínez-Lope, M. J.; Rasines, I. High Oxygen Pressure Preparation, Structural Refinement, and Thermal Behavior of RMn2O5 (R = La, Pr, Nd, Sm, Eu). *J. Solid State Chem.* **1997**, *129* (1), 105−112.
(37) Euzen, P.; Leone, P.; Gueho, C.; Palvadeau, P. Structure of NdMn2O5. *Acta Crystallogr. C* **1993**, *49* (11), 1875−1877.
(38) García-Flores, A. F.; Granado, E.; Martinho, H.; Urbano, R. R.; Rettori, C.; Golovenchits, E. I.; Sanina, V. A.; Oseroff, S. B.; Park, S.; Cheong, S.-W. Anomalous Phonon Shifts in the Paramagnetic Phase of Multiferroic RMn2O5 (R = Bi, Eu, Dy): Possible Manifestations of Unconventional Magnetic Correlations. *Phys. Rev. B* **2006**, *73* (10), No. 104411.
(39) Kolte, J.; Salame, P. H.; Daryapurkar, A. S.; Gopalan, P. Impedance and AC Conductivity Study of Nano Crystalline, Fine Grained Multiferroic Bismuth Ferrite ($BiFeO_3$), Synthesized by Microwave Sintering. *AIP Adv.* **2015**, *5* (9), No. 097164.
(40) Kirsch, A.; Murshed, M. M.; Litterst, F. J.; Gesing, T. M. Structural, Spectroscopic, and Thermoanalytic Studies on Bi2Fe4O9: Tunable Properties Driven by Nano- and Poly-Crystalline States. *J. Phys. Chem. C* **2019**, *123* (5), 3161−3171.
(41) Liu, J.; Lu, W.; Tian, B.; Hu, B.; Jin, L.; Shi, Y.; Li, L.; Wang, Z. Shape-Controlled Synthesis and Facet-Dependent Performance of Single-Crystal $Bi_{25}GaO_{39}$ Photocatalysts. *CrystEngComm* **2016**, *18* (40), 7715−7721.
(42) Shpanchenko, R. V.; Tsirlin, A. A.; Kondakova, E. S.; Antipov, E. V.; Bougerol, C.; Hadermann, J.; van Tendeloo, G.; Sakurai, H.; Takayama-Muromachi, E. New Germanates RCrGeO5 (R = Nd−Er, Y): Synthesis, Structure, and Properties. *J. Solid State Chem.* **2008**, *181* (9), 2433−2441.
(43) Durand, A.; Mentre, O.; Abraham, F.; Fukuda, T.; Elouadi, B. Crystal Structure of $ErAlGeO_5$ and Evidence of a Peculiar Double Coordination Sphere of Al(III) and Ge(IV) Cations. *Solid State Sci.* **2006**, *8* (2), 155−161.
(44) Muñoz, A.; Alonso, J. A.; Martínez-Lope, M. J.; Martínez, J. L. Synthesis, Structural, and Magnetic Characterization of a New Ferrimagnetic Oxide: $YFeMnO_5$. *Chem. Mater.* **2004**, *16* (21), 4087−4094.
(45) Alonso, J. A.; Martínez-Lope, M. J.; Casais, M. T.; Martínez, J. L.; Pomjakushin, V. Synthesis, Structural, and Magnetic Characterization of $YCrMnO_5$. *Eur. J. Inorg. Chem.* **2005**, *2005* (13), 2600−2606.
(46) Ashiotis, G.; Deschildre, A.; Nawaz, Z.; Wright, J. P.; Karkoulis, D.; Picca, F. E.; Kieffer, J. The Fast Azimuthal Integration Python Library: PyFAI. *J. Appl. Crystallogr.* **2015**, *48* (2), 510−519.
(47) Yang, X.; Juhas, P.; Farrow, C. L.; Billinge, S. J. L. XPDFsuite: An End-to-End Software Solution for High Throughput Pair Distribution Function Transformation, Visualization and Analysis. *arXiv (cond-mat)*. 13 Feb **2014**. DOI: 10.48550/arXiv.1402.3163 (accessed 2023−09−18).
(48) Fischer, P.; Frey, G.; Koch, M.; Könnecke, M.; Pomjakushin, V.; Schefer, J.; Thut, R.; Schlumpf, N.; Bürge, R.; Greuter, U.; Bondt, S.; Berruyer, E. High-Resolution Powder Diffractometer HRPT for Thermal Neutrons at SINQ. *Phys. B* **2000**, *276−278*, 146−147.
(49) Neuefeind, J.; Feygenson, M.; Carruth, J.; Hoffmann, R.; Chipley, K. K. The Nanoscale Ordered MAterials Diffractometer NOMAD at the Spallation Neutron Source SNS. *Nucl. Instrum. Methods Phys. Res. Sect. B* **2012**, *287*, 68−75.
(50) Coelho, A. A. TOPAS and TOPAS-Academic: An Optimization Program Integrating Computer Algebra and Crystallographic Objects Written in C++. *J. Appl. Crystallogr.* **2018**, *51* (1), 210−218.
(51) Pawley, G. S. Unit-Cell Refinement from Powder Diffraction Scans. *J. Appl. Crystallogr.* **1981**, *14* (6), 357−361.

(52) Rietveld, H. M. A Profile Refinement Method for Nuclear and Magnetic Structures. *J. Appl. Crystallogr.* **1969**, *2*, 65−71.
(53) Farrow, C. L.; Juhas, P.; Liu, J. W.; Bryndin, D.; Božin, E. S.; Bloch, J.; Proffen, T.; Billinge, S. J. L. PDFfit2 and PDFgui: Computer Programs for Studying Nanostructure in Crystals. *J. Phys.: Condens. Matter* **2007**, *19* (33), No. 335219.
(54) van Beek, W.; Safonova, O. V.; Wiker, G.; Emerich, H. SNBL, a Dedicated Beamline for Combined *in Situ* X-Ray Diffraction, X-Ray Absorption and Raman Scattering Experiments. *Phase Transit.* **2011**, *84* (8), 726−732.
(55) Clausen, B. S.; Steffensen, G.; Fabius, B.; Villadsen, J.; Feidenhans'l, R.; Topsøe, H. In Situ Cell for Combined XRD and On-Line Catalysis Tests: Studies of Cu-Based Water Gas Shift and Methanol Catalysts. *J. Catal.* **1991**, *132* (2), 524−535.
(56) Ravel, B.; Newville, M. *ATHENA, ARTEMIS, HEPHAESTUS*: Data Analysis for X-Ray Absorption Spectroscopy Using *IFEFFIT*. *J. Synchrotron Radiat.* **2005**, *12* (4), 537−541.
(57) Newville, M. Larch: An Analysis Package for XAFS and Related Spectroscopies. *J. Phys. Conf. Ser.* **2013**, *430*, No. 012007.
(58) Schindelin, J.; Arganda-Carreras, I.; Frise, E.; Kaynig, V.; Longair, M.; Pietzsch, T.; Preibisch, S.; Rueden, C.; Saalfeld, S.; Schmid, B.; Tinevez, J.-Y.; White, D. J.; Hartenstein, V.; Eliceiri, K.; Tomancak, P.; Cardona, A. Fiji: An Open-Source Platform for Biological-Image Analysis. *Nat. Methods* **2012**, *9* (7), 676−682.
(59) De La Peña, F.; Prestat, E.; Fauske, V. T.; Burdet, P.; Lähnemann, J.; Jokubauskas, P.; Furnival, T.; Nord, M.; Ostasevicius, T.; MacArthur, K. E.; Johnstone, D. N.; Sarahan, M.; Aarholt, T.; Taillon, J.; Pquinn-Dls; Migunov, V.; Eljarrat, A.; Caron, J.; Francis, C.; Nemoto, T.; Poon, T.; Mazzucco, S.; Actions-User; Tappy, N.; Cautaerts, N.; Suhas, Somnath; Slater, T.; Walls, M.; Winkler, F.; DENSmerijn Hyperspy/Hyperspy: Release v1.7.0, 2022.

https://doi.org/10.1021/acs.chemmater.3c01830
Chem. Mater. 2023, 35, 8664−8674